Dehydrogenative coupling of LLM-116 over copper-nickel-oxide nanoparticles：TEMPO-mediated homogeneous electrocatalysis

SCHOLARONE™
Manuscripts

Dehydrogenative coupling of LLM-116 over copper-nickel-oxide nanoparticles：TEMPO-mediated homogeneous electrocatalysis

Yuqiu Wang [a], Guangyuan Zhang [b], Aijia Tang [a], Ming Lu [a], Pengcheng Wang [a]*

[a] School of Chemistry and Chemical Engineering, Nanjing University of Science and Technology, Nanjing, 210094, PR China

[b] Gansu Yinguang Chemical Industry Group. Co. Ltd, Baiyin 730900. Gansu Province, China

E-mail: alexwpch@njust.edu.cn

Graphical Abstract:

☺ **Homogeneous oxidation**   ☺ **Room temperature and low cell voltage**

☺ **Clean electrons and recyclable TEMPO**   ☺ **No chemical waste**
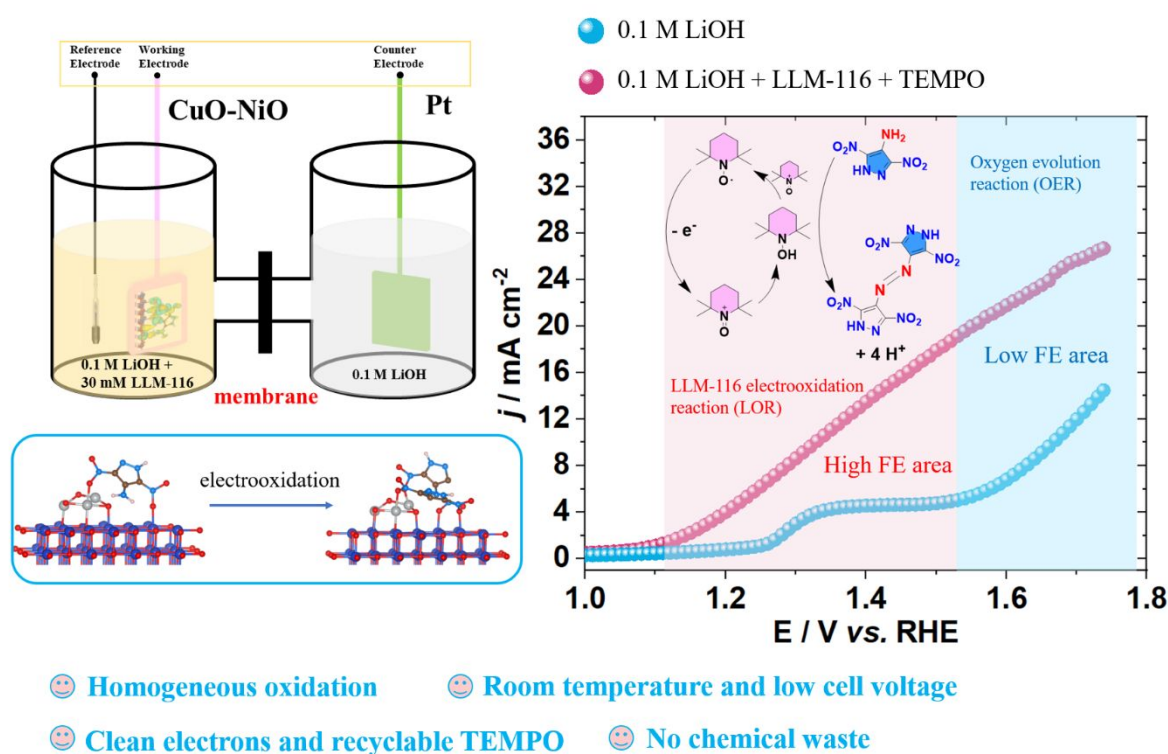
Abstract: Electrochemical oxidation can achieve remarkable selectivity through the meticulous optimization of electrode materials and the judicious selection of electrocatalytic mediators. The electrosynthesis of 1,2-Bis(3,5-dinitro-1H-pyrazol-4-yl) diazene (H$_2$NPA) attained a notably high Faradaic efficiency of 81.69% in 0.1 M LiOH at 1.65 V$_{RHE}$ with CuO-NiO spherical nanoparticles as the anode and TEMPO as the electrocatalytic mediator, effectively circumventing the environmental contamination and heterogeneous oxidation associated with conventional approaches. The doping of NiO proves advantageous in optimizing adsorption energy and surface charge density, thereby providing more active sites. Moreover, TEMPO aids in achieving favorable thermodynamics by providing a more suitable reduction potential, leading to the onset potential ahead by 150 mV. In-situ ATR-FTIR analysis and DFT calculations reveal that the active group -NH$_2$ initially couples to form -NH-NH- after deprotonation, subsequently undergoing dehydrogenation to yield H$_2$NPA. This study presents a novel strategy for the organic electrosynthesis of nitro-containing energetic materials, leveraging the synergistic catalysis of electrode materials and electrocatalytic mediators.

Keywords: organic electrosynthesis; selective oxidation; synergetic catalysis; energetic materials

1. Introduction

The urgent issues posed by high fossil fuel prices, energy security concerns, and climate change underscore the pressing need to accelerate the development of clean energy systems. In the realm of green chemistry, electrochemistry presents a distinctive avenue for selective oxidation. Typically, oxidation reactions involving an amino group as the active moiety utilize hydrogen as the terminal electron acceptor, resulting in H$_2$ as the only by-product.[1,2] In addition, the electron transfer rate and the selectivity of the reaction can be controlled by adjusting the reaction potential.[3-5] However, some special challenges still exist in organic electrosynthesis.[6] The fundamental principle of organic electrooxidation lies in the ability of the electrode to facilitate substrate dehydrogenation and coupling. This driving force originates from the heterogeneous phase reaction between the solid electrode and the substrate, which is subject to kinetic limitations.[7] However, reactions typically necessitate a high electrode potential, leading to the decomposition of unstable functional groups or the formation of unintended by-products under high voltages, which can be detrimental to the reaction. Moreover, heterogeneous oxidation lacks selectivity for functional groups beyond voltage control, and the electrode cannot govern the chemical reaction post-electron transfer.

The incorporation of an electrocatalytic mediator effectively addresses these issues by serving as an intermediary between the electrode and the substrate.[8,9] This mediator facilitates heterogeneous electron transfer at the electrode interface and accelerates the homogeneous oxidation of the substrate in the solution, thereby enhancing reaction kinetics.[10] Furthermore, the suitable electrocatalytic mediator can also selectively target reaction intermediates to further regulate side reactions.[11,12] Electrocatalytic mediators can be categorized into three types based on different catalytic mechanisms.[6,8] The first type involves modifying electron transfer processes to enable substrate oxidation not only at the electrode surface but throughout the entire solution. The second

type focuses on adjusting the rate of hydrogen atom transfer, facilitating faster substrate dehydrogenation to product conversion. The third type involves regulating the rate of electron transfer coupled with hydrogen (or other atom) transfer, as well as the rate of reactions catalyzed by transition metals. TEMPO belongs to the third category of electrocatalytic mediators and exhibits outstanding performance, making it widely employed in organic oxidation.[13,14] It catalyzes the dehydrogenation of hydrazobenzenes to azobenzenes,[15] as well as the conversion of aldehydes into nitriles.[16] However, its most typical application lies in catalyzing the selective oxidation of organic alcohols into aldehydes, ketones, and carboxylic acid compounds.[17,18] The work of Stahl S.S. et al. revealed a notable synergistic effect of Cu^{II} and TEMPO on the electrooxidation of alcohol compounds. Specifically, Cu^{II} was found to facilitate the conversion of TEMPOH to TEMPO and collaborate with it to regulate the oxidation of alcohol compounds.[19] The potential of the Cu/TEMPO catalyst system was observed to be 500 mV lower than that of the pure TEMPO system. Consequently, the Cu/TEMPO catalyst enables faster rates to be achieved even at lower driving forces.
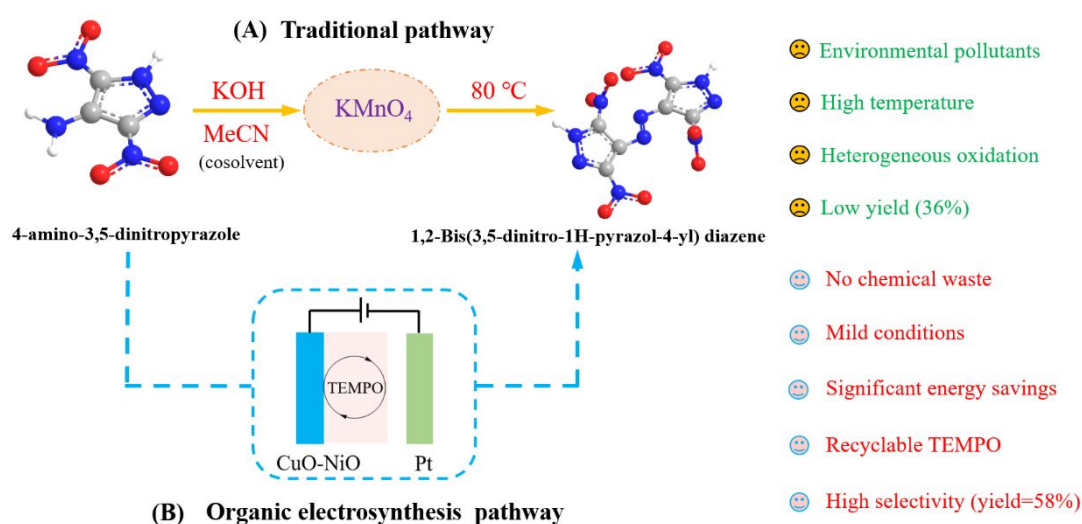
The selection of an appropriate electrode material plays a crucial role in achieving optimal yield and selectivity in organic electrosynthesis.[20] Electrodes significantly influence the dynamics and thermodynamics of electron transfer, thereby often determining the success or failure of the transformation. CuO serves as a common anode catalyst in oxidation coupling reactions. Research conducted by Choi K.S. et al. demonstrated that CuO exhibits superior selectivity for the HMFOR due to its limited competitive oxygen evolution reaction (OER) compared with other transition metal-based oxides.[21] In the field of ammonia electrochemical oxidation (AOR), CuO significantly facilitates the polymerization of -NH groups, leading to the formation of -NxHy.[22] Ma et al.'s work revealed stronger adsorption of 5AT on the surface of CuO, indicating that 5AT exhibits enhanced interaction with CuO, thereby promoting the formation of ZT.[23] Furthermore, as per Qiu et al., the Cu site of CuO, acting as the primary adsorption and reaction active site, preferentially binds to the N site of the furazan ring in DAF to initiate the oxidation coupling of DAF facilitated by •OH radicals.[24]

The interaction between the catalyst and substrate is crucial, largely depending on the atomic arrangement and electronic structure of the surface and interface.[25] However, the oxidation ability of CuO is weaker compared to other transition metals with higher valence states. The incorporation of other active atoms has synergistic effects on substrate adsorption and the electron transfer of reaction intermediates, which holds significant promise for Cu-based materials in the realm of electrooxidation. NiO demonstrates a robust adsorption capacity, with its affinity for N atoms even surpassing that of Pt in AOR.[22,26] Moreover, the introduction of NiO can modulate the adsorption

capacity of various reactive species.[27]

1,2-Bis(3,5-dinitro-1H-pyrazol-4-yl) diazene (H$_2$NPA) is a heat-resistant explosive containing typical azo bonds. Due to the low solubility of 4-amino-3,5-dinitropyrazole (LLM-116) in strong alkali solutions, a non-homogeneous system forms when KMnO$_4$ is used as the oxidant, resulting in a yield of approximately 36%.[28] Moreover, environmental pollution arising from the use of strong oxidants presents a significant challenge, underscoring the need for optimizing the production process.

In this study, CuO-NiO spherical nanoparticles were employed as the anode in 0.1 M LiOH to catalyze the LLM-116 electrooxidation reaction (LOR) for synthesizing H$_2$NPA. TEMPO was utilized as an electrocatalytic mediator to prevent heterogeneous oxidation, thereby effectively reducing the onset potential (Scheme 1). The catalytic effects of the composite metal electrode and TEMPO on LOR were investigated separately, and the catalytic mechanism of TEMPO was elucidated from a thermodynamic perspective. The reaction process of LOR was analyzed using in-situ infrared spectroscopy and electrochemical testing. Density functional theory (DFT) was employed to analyze the reaction pathways. Finally, other derivatives of H$_2$NPA were synthesized via electrochemical oxidation, and their thermal properties were analyzed by DSC. This study contributes novel insights into the organic electrosynthesis of energetic materials, focusing on two key aspects: optimizing electrode materials and selecting appropriate electrocatalytic media.

(A) Traditional pathway

KOH
MeCN (cosolvent)
KMnO$_4$
80 °C

4-amino-3,5-dinitropyrazole

1,2-Bis(3,5-dinitro-1H-pyrazol-4-yl) diazene

☹ Environmental pollutants
☹ High temperature
☹ Heterogeneous oxidation
☹ Low yield (36%)

☺ No chemical waste
☺ Mild conditions
☺ Significant energy savings
☺ Recyclable TEMPO
☺ High selectivity (yield=58%)

TEMPO
CuO-NiO   Pt

(B) Organic electrosynthesis pathway

Scheme 1 (A) Traditional pathway for the synthesis of 1,2-Bis(3,5-dinitro-1H-pyrazol-4-yl) diazene by KMnO$_4$ in 80 °C. (B) Organic electrosynthesis at 1.65 V$_{RHE}$ by CuO-NiO assisted with TEMPO.

2. Experimental sections

Materials. LLM-116 was synthesized using 4-Chloropyrazole as raw material according to the previously reported method.[29] Other reagents and solvents are analytical grade purchased from

commercial sources and used directly.

Synthesis of CuO-NiO materials. Dissolve 0.5 mmol nickel (II) nitrate hexahydrate and 2 mmol copper (II) nitrate tetrahydrate in a mixture of 10 mL ethanol and 40 mL DI water. The precursor solution was prepared by adding 200 mg sodium dodecyl sulfate (SDS) and 120 mg carbon black powder into 10 mL NH_4OH (0.4 M) solution.[30] After stirring for 30 min, the mixture was refluxed at 80℃ for 1 hour, centrifuged and dried after cooling, ground into uniform powder, and annealed at 350 ℃ for 2 h. CuO and NiO powders were synthesized by the same method.

Electrochemical testing. Electrochemical testing was performed using CHI660 electrochemical workstation, linear sweep voltammetry (LSV) curves and Cyclic Voltammetry (CV) curves were tested using a three-electrode system in a segmented H-type electrolytic cell. Nifon and ethanol were used to configure 2 wt% carbon black, CuO and CuO-NiO, and coated on a 1 cm^{-2} carbon cloth as working electrodes, respectively. The electrode was compared with platinum plate and the electrode was Hg/HgO. With 0.1 M LiOH as the electrolyte, all curve were tested at a sweep speed of 10 mV/s at room temperature with constant agitation. The frequency for impedance measurement ranged from 0.01 Hz to 10 KHz. The standard hydrogen electrode potential in the results was converted by the formula.

$$E_{RHE} = E_{Hg/HgO} + 0.098 + 0.059 \text{ pH}$$

Electrosynthesis of H₂NPA. The electrosynthesis of H₂NPA is carried out in an H-type electrolytic cell separated by a proton exchange membrane to avoid possible reduction of the nitro group. CuO-NiO was used as the anode for electrooxidation coupling, and Pt was used as the electrode for electrochemical hydrogen evolution reaction in the cathode chamber. 0.03 M LLM-116 and equimolar TEMPO were added to 0.1 M LiOH for constant voltage oxidation at 1.65 V_{RHE} for 3 h, with Hg/HgO as the reference electrode, the yellow solution in the anode chamber gradually turned red. At the end of the reaction, the pH of the solution was adjusted to 1, and the solution turned orange. After the water was removed with the oil pump and a small amount of ethanol was added to remove the inorganic salt, the product was separated by the expanding agent (EA: PE = 1: 4), and then purified by the expanding agent (EA: PE = 1: 2).

Testing and characterization of H₂NPA. High performance liquid chromatography (LC-20AT) was used to monitor the reaction conversion and product purity, and the concentration of the product was obtained by the liquid phase standard curve. In-situ infrared testing was performed by Electrochem IR (Ling Lu) to monitor the changes of functional groups during the reaction, thermal analysis of the products was performed by DSC (DSC 204 Phoenix), and molecular structure was confirmed by single crystal testing. Molecular weight was tested using mass spectrometry (Thermo. Q Exactive Focus). The molecular structure is determined by single crystal X-ray diffractometer,

which was carried out on a Bruker D8 QUEST diffractometer with microfocus Ius 2.0 Mo-Ka radiation (λ=0.71073 Å) at 296(2) K.

Calculation formula.

$$\text{LLM-116 conversion (\%)} = \frac{\text{mol of LLM-116 consumed}}{\text{mol of initial LLM-116}} \times 100\% \tag{1}$$

$$\text{Yield of product (\%)} = \frac{\text{mol of H}_2\text{NPA formed}}{\text{mol of H}_2\text{NPA theoretically formed}} \times 100\% \tag{2}$$

$$\text{FE (\%) for H}_2\text{NPA production} = \frac{\text{mol of H}_2\text{NPA formed}}{\text{mol of total electrons passed/4}} \times 100\% \tag{3}$$

Electrosynthesis of other H$_2$NPA derivatives.

Li$_2$NPA. CuO-NiO and Pt were used as the anode and cathode, respectively, in an H-type electrolytic cell. 0.03 M LLM-116 and equimolar TEMPO were added to 0.1 M LiOH for constant voltage oxidation at 1.65 V_{RHE} for 3 hours. The precipitated dark red spherical particles are Li$_2$NPA.

K$_2$NPA. Using the same method as for the synthesis of Li$_2$NPA, replacing 0.1M LiOH with 0.1M KOH, the red needle-shaped crystals precipitated after the reaction are K$_2$NPA.

Guanidinium. CuO-NiO and Pt were used as the anode and cathode, respectively, in an H-type electrolytic cell. 0.03 M LLM-116, equimolar TEMPO, and equimolar guanidine hydrochloride were added to 0.1 M LiOH for constant voltage oxidation at 1.65 V_{RHE} for 3 hours. The precipitated yellow solid is guanidinium.

Amino guanidinium. Using the same method as for the synthesis of guanidinium, replacing guanidine hydrochloride with aminoguanidine hydrochloride, the yellow solid precipitated after the reaction is amino guanidinium.

Hydrazine. Using the same method as for the synthesis of guanidinium, replacing guanidine hydrochloride with hydrazine hydrate, the deep red solid precipitated after the reaction is hydrazine.

Results and discussion

Characterization of CuO-NiO materials

Scanning electron microscopy (SEM) and high-resolution transmission electron microscopy (HRTEM) were employed to examine the morphology and microstructure of the CuO-NiO samples.[31,32] The SEM and TEM images revealed the presence of coral-like nano-spherical particles with an average size of 33.13 ± 8.86 nm (Fig. 1A-1C). This phenomenon is ascribed to the electrostatic fine dispersion effect of nanoparticles induced by the surfactant SDS.[30] The concentrations of Cu (15.19 wt.%) and Ni (0.27 wt.%) in the catalyst were determined using energy dispersive X-ray (EDX) spectroscopy (Fig. S1). High-angle annular dark-field imaging scanning transmission electron microscopy (HAADF-STEM) validated the nano-spherical particle morphology and elemental distribution of the CuO-NiO material, depicted in Fig. 1D-1F. The elements Cu, Ni, and O exhibited uniform distribution on the carbon black substrate, with the

individual and dual nanosphere elemental distributions illustrated in Fig. S2 and Fig. S3.

The crystal structure of CuO-NiO was assessed using X-ray powder diffraction (XRD). In Fig. 1H, the distinct diffraction peaks of CuO-NiO corresponded to the crystal planes of CuO (11-1), CuO (111), and CuO (20-2). The presence of Cu_2O and NiO was evidenced by 2θ values of 29.5, 36.4, 42.3, and 52.4° (Cu_2O, JCPDS 05-0667) and 2θ values of 37.2, 43.3, 62.9, 75.4, and 79.4 (NiO, JCPDS 47-1049). The weak intensity of the NiO diffraction peak can be attributed to the low Ni loading content. HRTEM images revealed well-defined lattice fringes with interplanar spacings of 0.252, 0.232, and 0.209 nm, corresponding to CuO (11-1), CuO (111), and NiO (200) planes, respectively, consistent with the XRD findings (Fig. 1I and Fig. S4).
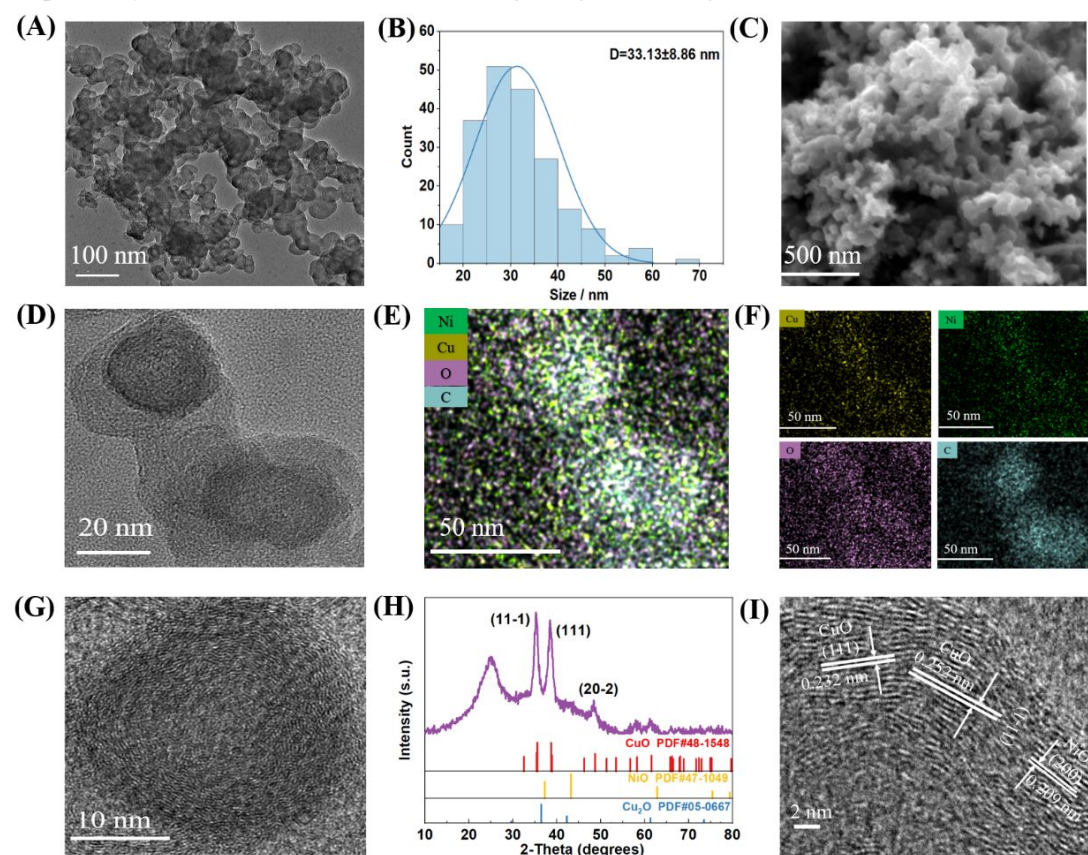

Fig. 1 (A) TEM, (B) particle size distribution and (C) SEM of CuO-NiO materials. (D) HRTEM and (E-F) EDX mapping images of the CuO-NiO. (G) Individual nanosphere particles. (H) XRD analysis. (I) HRTEM lattice analysis.

To ascertain the surface valence state and local microenvironment of CuO-NiO, as well as to investigate the electron changes during electrochemical synthesis, X-ray photoelectron spectroscopy (XPS) was employed to analyze CuO-NiO before and after LOR. Prior to the electrochemical synthesis, a Cu^I peak appeared at 933.6 eV (Fig. 2A), while in the post-LOR samples, the emergence of a Cu^{II} peak at 934.5 eV signifies the presence of CuO (Fig. 2D). Similarly, in the case of Ni 2p, the intensity of Ni^{2+} at 855.58 and 873.5 eV surpasses that of Ni^{3+} at 857.5 and 875.1 eV before LOR (Fig. 2B), suggesting that NiO predominates as the form of nickel on the

electrode surface. Subsequently, following LOR, conversion of Ni^{2+} to Ni^{3+} occurs due to electron loss, resulting in the prevalence of Ni^{3+} (Fig. 2E). Furthermore, the OH^- peak in the O 1s spectrum after LOR experiences a shift from 529.6 eV to 529.8 eV (Fig. 2C and Fig. 2F), indicating the adsorption of OH^- species in alkaline solutions.[22] Consequently, Cu^{2+} and Ni^{3+} are present on the electrode surface, serving as the active sites for LOR throughout the entire electrochemical synthesis process.
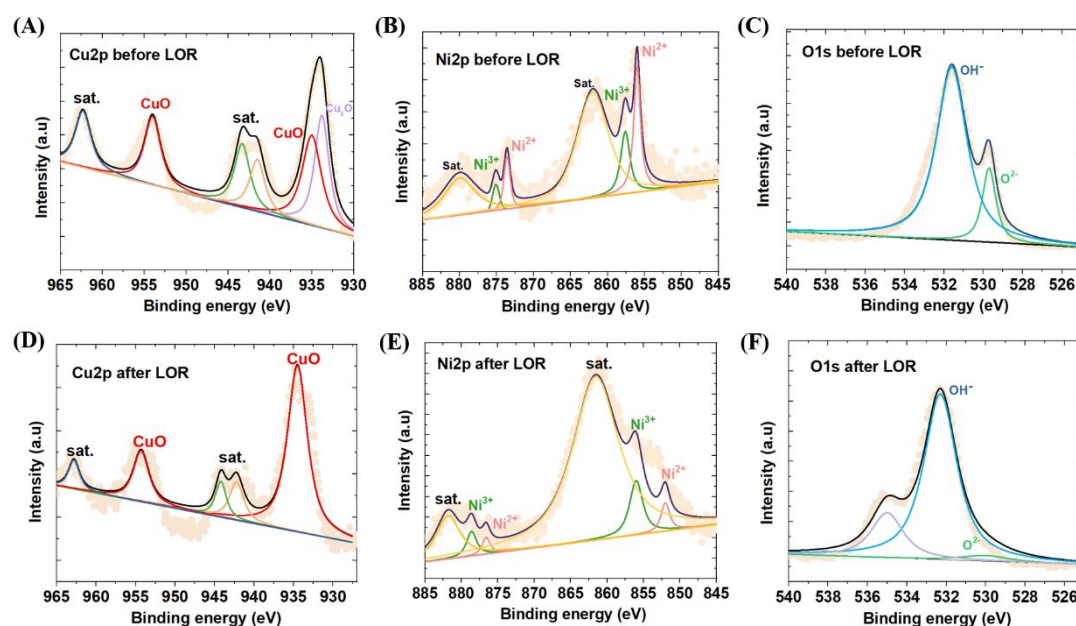

Fig. 2 (A-C) XPS spectra of Ni 2p, Cu 2p and O 1s before LOR, (D-F) after LOR.

Catalytic effect of electrode materials

LLM-116 exhibits poor solubility in strong alkaline solutions, particularly when the pH exceeds 13. Zhou et al. employed acetonitrile as a cosolvent during the synthesis of H_2NPA using KMnO4,[28] which may account for the low yield. In our research, $^nBu_4NBF_4$ was used as an electrolyte for electrosynthesis in the acetonitrile system. However, the signal peak of H_2NPA was not detected via High-performance liquid chromatography (HPLC), as depicted in Fig. S5. Standard curves for both the raw material LLM-116 and the product H_2NPA were separately generated using HPLC (Fig. S6-S7). Although the essence of electrochemical synthesis and chemical synthesis is characterized by redox reactions, the realization form differs: the former involves electron transfer, while the latter relies on strong oxidants. Therefore, selecting an appropriate alkali solution to achieve a homogeneous reaction represents one method for enhancing the yield.

Comparing the solubility of LLM-116 in different alkali environments, LiOH is the optimal choice, exhibiting superior substrate dissolution compared to KOH and NaOH at equivalent concentrations. The electrochemical properties of the material were assessed using a three-electrode system in 0.1 M LiOH (pH = 13) electrolyte. As depicted in the LSV curve shown in Fig. 3A, CuO-

NiO (1.24 V_{RHE}) exhibited a lower onset potential for LOR compared to CuO (1.29 V_{RHE}) and NiO (1.27 V_{RHE}).

The current density of CuO-NiO at 1.7 V_{RHE} is more than twice that of the other two materials (Fig. 3B), confirming that NiO doping demonstrates superior catalytic effects on substrate oxidation. Additionally, the charge transfer behavior of LOR was probed using electrochemical impedance spectroscopy (EIS). When the interfacial reaction on the electrode is constrained solely by the charge transfer process (reaction kinetics) rather than diffusion processes (mass transfer), the EIS spectra typically display a semicircular shape.[25] As shown in Fig. 3C, the decrease in the size of the semicircle after NiO doping signifies a reduction in resistance, effectively accelerating the rate of charge transfer facilitated by NiO doping. This diminished reaction resistance is further evident in the Tafel slope (Fig. S8), confirming the favorable impact of NiO doping on improved reaction kinetics and catalytic activity.[33]

Through a comparison of the obtained LSV in the presence and absence of 30 mM LLM-116 in 0.1 M LiOH, the ability of CuO-NiO electrodes to selectively catalyze oxidation is assessed.[34] In the absence of LLM-116, only the OER occurs. As depicted in Fig. 3D, the obtained LSV reveals an onset potential of 1.6 V_{RHE} for OER. With the presence of 30 mM LLM-116, the onset potential shifts to 1.25 V_{RHE}, indicating that CuO-NiO facilitates the oxidation of LLM-116 more readily due to its weaker response towards OER.

The CV curves of CuO-NiO before and after the addition of the substrate are illustrated in Fig. 3E. The CV with LLM-116 displays a distinct oxidation peak at 1.44 V_{RHE}. When compared with the CV of CuO shown in Fig. 3F, NiO doping leads to the emergence of an initial current at 1.25 V_{RHE} for CuO-NiO (green line in Fig. 3E). This indicates the transition of Ni^{2+} to Ni^{3+} through electron loss. According to the research of Zou et al., this transition signifies a proton-coupled electron transfer (PCET) process, providing unoccupied orbitals for electron transfer.[35] It is observed that Ni^{3+} is unable to oxidize water, and once Ni^{2+} transitions to Ni^{3+}, LLM-116 is promptly electrolyzed. This also indicates that within the reaction system, only LLM-116 can be attacked by Ni^{3+} in the electrode material, while OER requires Ni^{a+} ($a \geq 4$) to occur. This underscores the selective oxidation of materials, demonstrating a significant advantage of LOR over the competitive OER. The work of Wang et al. illustrates that the formation of high-valence nickel species during the electrocatalytic process enhances anodic reaction activity, attributed to the spatial distance of metal sites regulating substrate adsorption energy, thereby reducing the reaction energy barrier.[25]

The investigation into the electrochemical surface areas (ECSAs) of the materials unveiled a larger ECSA for CuO-NiO compared to carbon black and CuO (Fig. S9).[36] This indicates that the

doping of NiO is conducive to generating more electrocatalytic active sites. LOR in 0.1 M LiOH has a competitive advantage compared with 0.1 M KOH electrolyte, demonstrated specifically by a difference in current response of 12 mA between LOR and OER at 1.74V, with an onset potential difference of 280 mV in LiOH (Fig. 3D). In contrast, the current response difference is 6 mA with an onset potential difference of 240 mV in KOH, as depicted in Fig. S10. Additionally, the voltage required for the LOR under the same constant current (5 mA) was compared, and the voltage dropped after 0.03 M LLM-116 was injected into 0.1 M LiOH, indicating that LOR can occur at a lower potential (Fig. 3G). The potential drop is larger for CuO-NiO (530 mV) than for CuO (470 mV), which suggests that NiO doping is more beneficial for catalytic dehydrogenation coupling.

The effect of substrate concentration on LOR was investigated through LSV tests, where 0.02, 0.03, 0.04, and 0.05 M LLM-116 were introduced into 0.1 M LiOH electrolyte. The LSV tests indicated that the substrate concentration of 0.03 M exhibited the best catalytic activity for oxidative coupling (Fig. 3H). HPLC was utilized to monitor the product formation within 35 minutes, and the product concentration was determined from the peak area of the standard curve (Fig. S6). Consistent with the LSV tests, the product concentration generated at the substrate concentration of 0.03M was higher than that of other substrates, and the kinetic reaction rate was faster.
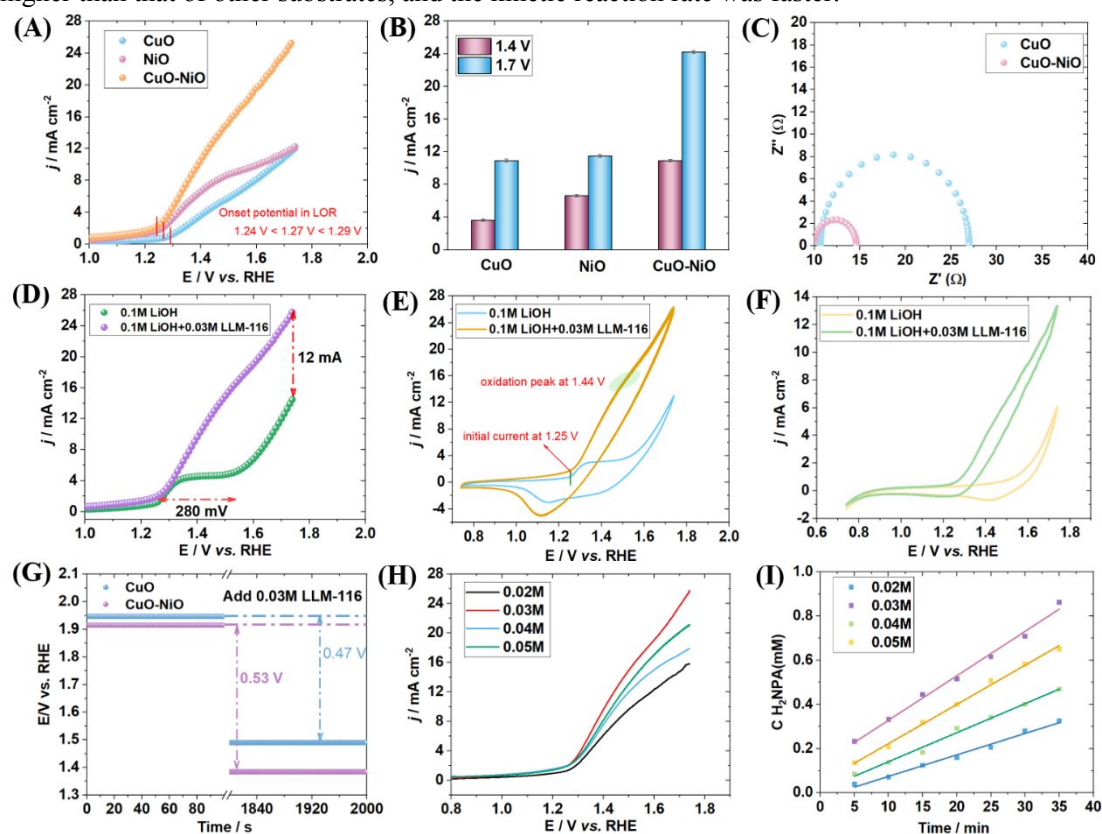

Fig. 3 (A) LSV curves of the CuO, NiO and CuO-NiO for LOR in 0.1M LiOH. (B) Current density of LOR at 1.4 V_{RHE} and 1.7 V_{RHE} for different electrode materials. (C) Resistance of LOR before and after NiO doping. (D) Changes in current density and LOR onset potential before and after the addition of substrate in 0.1 M LiOH by CuO-NiO. (E) CV curves of CuO-NiO before and after adding substrate in 0.1M LiOH. (F) CV curves of CuO before

and after adding substrate to 0.1 M LiOH. (G) Voltage required for LOR to occur before and after NiO doping. (H) LSV curves at different substrate concentrations. (I) The concentration of LOR product as a function of time at different substrate concentrations measured by HPLC.

The catalytic role of TEMPO

The applicability of TEMPO was investigated using CV tests.[37,38] Initially, the CV curve of TEMPO itself was observed, revealing that the reduction current equals the oxidation current, indicating a reversible reaction has occurred (Fig. 4A). This also signifies that TEMPO is a stable electrocatalytic medium, as the activity of any N-oxo catalyst incapable of providing fully reversible oxidation pairs tends to be inferior.[39]

After adding the substrate, CV was measured and a gradual decrease in the reverse current was observed, indicating that TEMPO had initiated the oxidation of the substrate (Fig. 4B). This observation also suggests that TEMPO loses electrons at the CuO-NiO anode, thereby acquiring oxidizing capability.

Subsequently, TEMPO was added when CuO-NiO catalyzed LOR, and it was pleasantly discovered that the onset potential shifted ahead by 150 mV (Fig. 4C), accompanied by a slight increase in response current. This phenomenon becomes more pronounced with higher amounts of TEMPO added, indicating the catalytic effect of TEMPO on LOR. The minimum voltage required for the LOR was compared under a constant current of 5 mA by the E-T test. Upon injection of the substrate, a decrease in reaction voltage was noted (Fig. 4D). With a greater voltage drop observed upon the addition of TEMPO, signifying that the reaction could occur at a lower potential with TEMPO present, resulting in a lower reaction energy barrier.

Finally, the relationship between TEMPO and CuO-NiO was investigated. As shown in Fig. 4E, when using carbon black as the electrode, the reaction was solely catalyzed by TEMPO, whereas with CuO-NiO as the electrode, the onset potential shifted ahead by 100 mV. Combined with Fig. 4C, this indicates a synergistic relationship between CuO-NiO and TEMPO in LOR. Drawing from studies on the cooperative catalysis of Cu/TEMPO in the oxidation of organic alcohols, it is inferred that TEMPO is initially oxidized by Cu^{2+}/Ni^{3+} and then cooperatively catalyzes the amino of LLM-116 dehydrogenation and coupling along with CuO-NiO.[19,40]
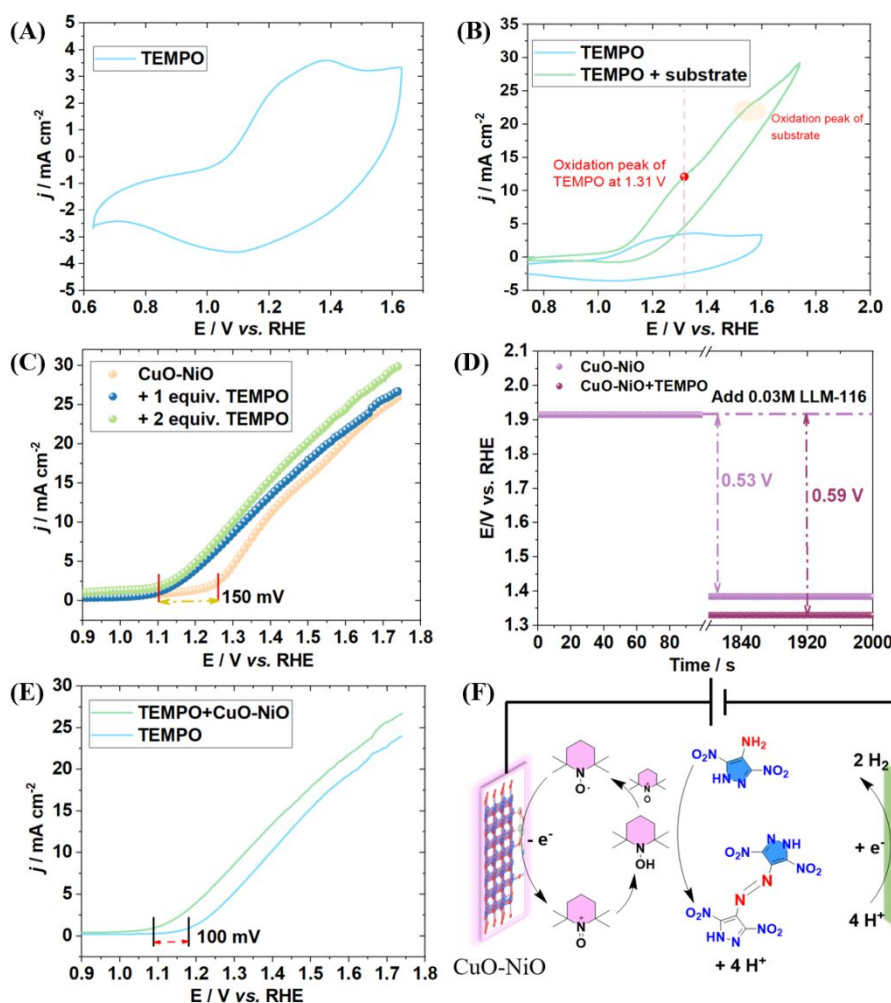
Fig. 4 (A) CV curve of TEMPO. (B) CV curves for the addition of substrates to TEMPO. (C) Changes of onset potential after adding different amounts of TEMPO when CuO-NiO catalyzed LOR. (D) Changes of voltage drop for LOR before and after the addition of TEMPO. (E) A synergistic relationship between CuO-NiO and TEMPO in LOR. (F) Supposed mechanism of LOR catalyzed by TEMPO cooperatively with CuO-NiO.

Reaction progress of LOR

The selective generation of H_2NPA and the Faradaic efficiency (FE) are critical parameters in LOR. In the experiment, 0.03 M LLM-116 and an equimolar amount of TEMPO were added to 0.1 M LiOH electrolyte, and constant voltage oxidation was carried out for 3 hours at 1.65 V_{RHE}, with Hg/HgO as the reference electrode. The yellow solution in the anode chamber gradually turned red visibly over time, as shown in the i-t curve depicted in Fig. 5A. The caculation for conversion, yield, and FE are provided in equations 1-3, respectively. An impressive conversion rate of 81.5% was achieved by HPLC when CuO-NiO was used as the electrode with the addition of the catalytic agent TEMPO (Fig. 5B). To eliminate the influence of the substrate and to showcase the catalytic oxidation capability of the metal material itself, carbon black and CuO electrodes were prepared using the same method for LOR. The conversion rates of other materials are provided in Fig. S12-S14, and the i-t curves are displayed in Fig. S15-S17. As depicted in Fig. 5C, the FE with carbon

black was 56.82%, and the yield was 25%. When CuO-NiO was used as the electrode with TEMPO as the electrocatalytic medium, the FE increased to 81.69% with a yield of 58%. All data demonstrated significant improvement compared to using CuO-NiO alone, confirming that the synergistic effect between CuO-NiO and TEMPO accelerated the selective generation of H_2NPA and the oxidation rate of the substrate.

To further investigate the reaction kinetics during the electrochemical catalytic process, the Bode plots were analyzed before and after NiO doping using EIS, as illustrated in Fig. 6D-6E.[41,42] The phase angle of the CuO-NiO catalytic system is smaller than that of the CuO system under the same voltage, indicating enhanced catalytic reaction kinetics due to NiO doping. Additionally, as the potential increases, a noticeable shift in the phase angle of CuO and CuO-NiO in the low-frequency region was observed at 1.3 V_{RHE} (denoted by the purple circles in the diagram), indicating substrate oxidation coupling at this specific potential. Notably, the phase angle value of CuO-NiO in the high-frequency region is notably lower than that of CuO, indicating superior reaction kinetics of the composite material. Furthermore, the Nyquist plots of OER and LOR tested at different voltages also indicate that LOR takes precedence over OER (Fig. S21).[43]

To track the dynamic behavior of intermediates during the electrosynthesis of H_2NPA, in-situ ATR-FTIR analysis was carried out (Fig. S18).[44,45] When CuO-NiO was employed as the anode, a progressively conspicuous red-shift anti-absorption signal emerged at 3340 cm^{-1} with increasing voltage, indicating the formation of -NH.[46] It is hypothesized that the active group $-NH_2$ of the substrate undergoes oxidation and proton abstraction to generate the intermediate -NH, representing the primary step in the electrochemical synthesis of H_2NPA (Fig. 5F). While the appearance of the -NH signal began at 1.3 V_{RHE} for CuO (Fig. 5G), a more robust transmittance signal was detected at 1.1 V_{RHE} following NiO doping, suggesting a swifter generation and wider distribution of intermediates after NiO doping. The progressively enhanced transmittance signals at 1540 cm^{-1} and 1470 cm^{-1} result from the generation of -N=N-, as confirmed by the OER spectra in Fig. S16, affirming that these peaks do not correspond to infrared signals from water. In comparison with the transmittance intensity of CuO at these peaks, NiO doping expedites the intermediate coupling and -N=N- formation rate. Coupling represents the second pivotal phase in the electrosynthesis of H_2NPA. The sequence of whether the -NH- of intermediate undergoes deprotonation prior to coupling or initially forms -NH-NH- through coupling followed by dehydrogenation necessitates determination based on density functional theory (DFT) calculations of the reaction potential. In-situ ATR-FTIR testing not only captures the deprotonation of the active group $-NH_2$ to produce -NH- and the coupling process forming -N=N-, but also indicates, via potential and transmittance intensity measurements, that NiO doping enhances the material's surface activity, improves reaction

kinetics, accelerates the oxidation rate in the electrosynthesis of H$_2$NPA, promotes an increase in the coupling rate, and further enhances the selective conversion capability of LLM-116.

Ultimately, the structure of the compound was elucidated utilizing X-ray single crystal diffraction. Fig. 5H illustrates the single crystal structure of H$_2$NPA synthesized under 1.65 V$_{RHE}$, with a decomposition temperature of 221.87 ℃ determined by DSC at a heating rate of 10 ℃/min. As depicted in Fig. S22, mass spectrometry also confirmed the correctness of the molecular structure (M/Z = 341). The derived compounds synthesized by electrooxidation were verified by their decomposition temperatures (Td), with the highest Td observed for the potassium salt at 316.1 °C. The new compound Li$_2$NPA has a Td of 241.7 °C. Among the non-metallic salts, the highest Td is for the guanidine salt at 305.3 °C, followed by the aminoguanidine salt at 195.8 °C, and lastly the hydrazine salt at 157.6 °C.
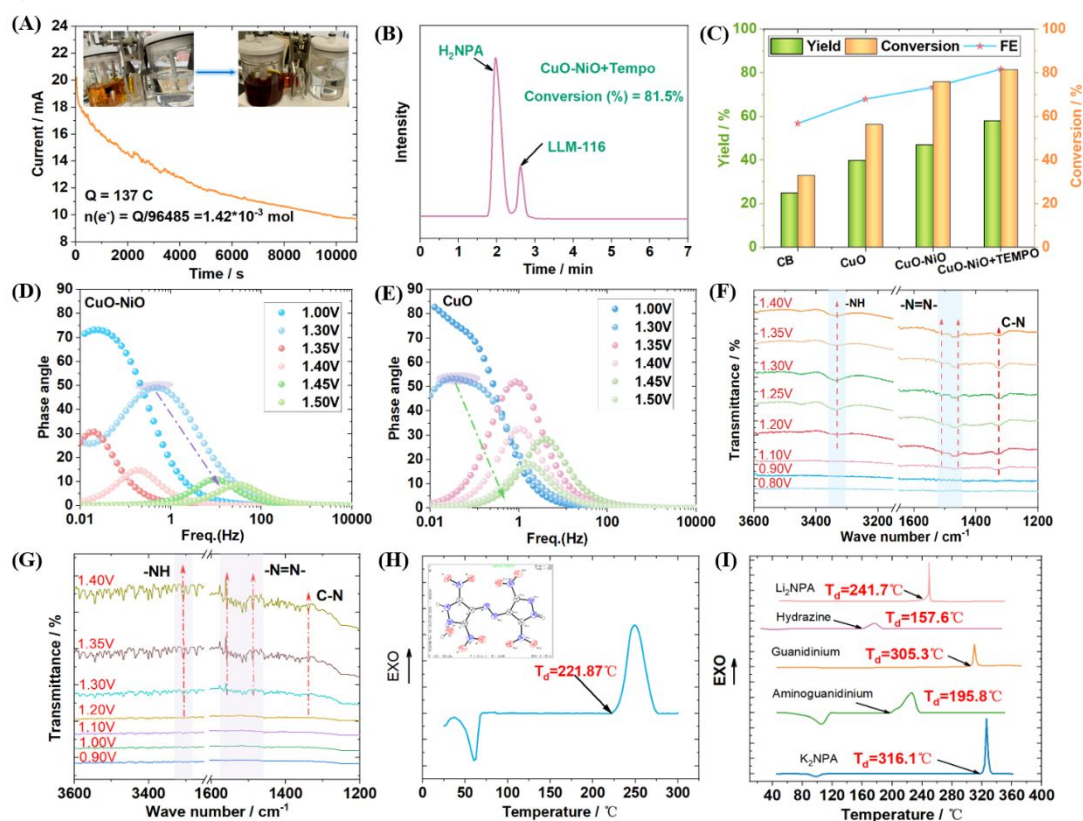

Fig. 5 (A) I-T curve of LOR at 1.65 V$_{RHE}$ for 3 h with CuO-NiO as the anode and TEMPO as the catalyst. (B) The conversion rate achieved by HPLC in CuO-NiO / TEMPO system. (C) The conversion rate, yield, and the FE of LOR under different materials. (D) The Bode plots of LOR after NiO doping using EIS. (E) The Bode plots of LOR before NiO doping using EIS. (F) ATR-FTIR analysis of LOR with CuO-NiO, (G) with CuO. (H) Decomposition temperature of H$_2$NPA and (I) other derivatives determined by DSC under a heating rate of 10 °C/min.

Reaction mechanism of LOR

Although the experimental observations mentioned above have demonstrated the catalytic effects of CuO-NiO and TEMPO on LOR, further investigation is needed to gain a deeper understanding of the catalytic mechanism and the rate-determining step of LOR. Firstly, DFT calculations are used

to study how composite electrode materials show advantages in catalyzing substrate oxidation in the system without TEMPO.

The adsorption energy and surface charge density of the substrate was evaluated pre- and post-NiO doping, alongside an investigation into the choice of reaction pathways.[47] The model of CuO and CuO-NiO, depicted in Fig. 6A, illustrates a shift in the adsorption site of compound 1 following NiO doping, resulting in an increase in adsorption energy from -0.43 to -1.58 eV (Fig. 6B) and a rise in the differential charge density between the compound and the surface from 0.31 to 0.57 e⁻ (Fig. 6C).

The incorporation of NiO introduces an increased number of active sites, which enhances the contact area between CuO and compound 1, thereby amplifying their mutual interactions. This augmented interaction results in a significant increase in adsorption energy, making compound 1 more readily adsorbed onto the CuO-NiO surface. The elevation in differential charge density indicates enhanced electron transfer between CuO-NiO and compound 1.[34] Studies suggest that the redistribution of surface charges on the material can further optimize the adsorption of CuO-NiO onto the substrate.[27] The additional active sites generated by NiO doping provide extra adsorption locations for reaction intermediates, facilitating electron transfer alongside compound 1. This electron exchange may lead to a partial rearrangement of the charge within molecule 1, strengthening the bond with the CuO-NiO interface. Consequently, the improved adsorption energy and charge transfer facilitated by NiO doping create more favorable conditions for the reactivity of compound 1 at the interface. These heightened interactions and electron transfers play a crucial role in activating compound 1 and catalyzing its interaction with other reactants on the CuO-doped NiO surface.

(A)

● Cu   ● Ni   ● O   ● C   ● N   ● H

(B)

Adsorption Energy (eV)

-0.43 (CuO)   -1.58 (NiO-CuO)

(C)

0.31 e⁻   CuO

0.57 e⁻   CuO-NiO

(D)

1   2   3   4   5

Reaction Energy (eV)

— CuO
— NiO-CuO

Reaction Pathway

Reaction pathway

$2 \,\text{N-O}\cdot + Cu^{2+} + Ni^{3+} \longrightarrow 2\,\text{N-O} + Cu^{+} + Ni^{2+}$
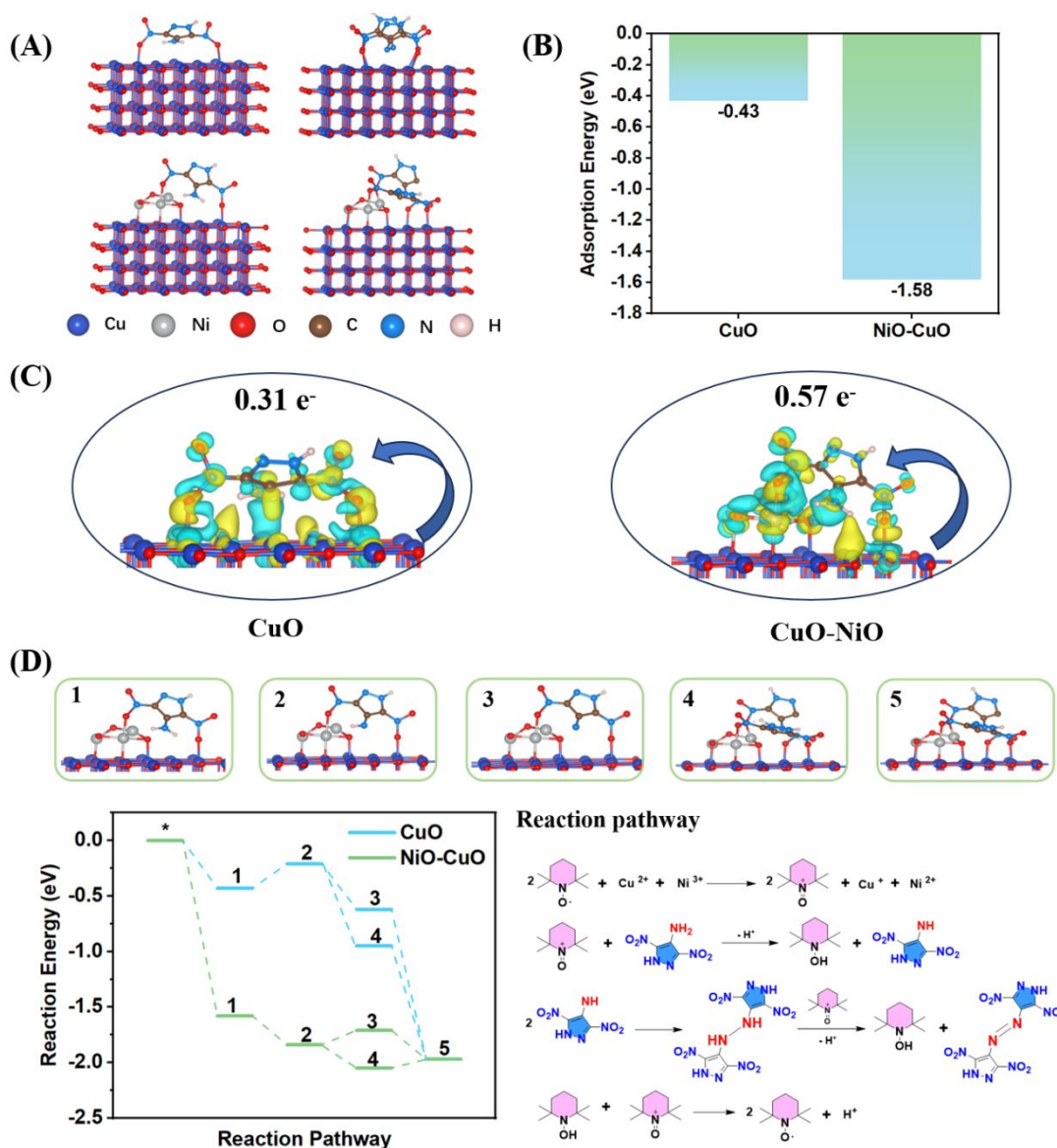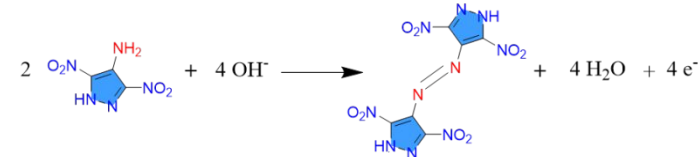
Fig. 6 (A) The model of CuO and CuO-NiO. (B) The adsorption energy and (C) the surface charge density of the substrate pre- and post-NiO doping. (D) An investigation into the choice of reaction pathways.

Upon NiO doping in CuO, the initial dehydrogenation free energy of compound 1 decreases from 0.22 eV to -0.26 eV, indicating a more favorable removal of a hydrogen atom from the amino group on the NiO-doped surface. The introduction of NiO brings forth supplementary active sites, enlarges the pool of adsorption sites for reaction intermediates, and heightens reaction efficacy via electron transfer with compound 1. Consequently, NiO doping reduces the free energy associated with the initial dehydrogenation, thus facilitating the removal of a hydrogen atom from the amino group. Free energy calculations reveal that the energy profile of pathway 2 (coupling preceding dehydrogenation) is lower than that of pathway 1 (dehydrogenation preceding coupling), indicating a preference for pathway 2 on the NiO-doped interface. This preference may arise from a smoother generation of intermediate 4 compared to intermediate 3 on the NiO-doped surface, possibly due to either a more stable transition state configuration in coupling reactions or a reduced activation

energy requirement in coupling reactions. Thus, the preference for pathway 2 primarily stems from its reduced free energy on the NiO-doped platform, making it more favorable for the progression of the reaction. Based on these results, we deduce that the crucial step governing substrate oxidation coupling is the formation of compound 2, with the speed of proton extraction being a critical aspect that NiO doping effectively enhances.

Table 1 Thermodynamic potentials of LOR and some typical oxidants.

	substrate oxidation	E^{θ} (V vs NHE)
a		8.17×10^{-25} V
	oxidant reduction	E^{θ} (V vs NHE)
b	$2\,H^+ + 2\,e^- \leftrightharpoons H_2$	0.00 V
c	$O_2 + 4\,H^+ + 4\,e^- \leftrightharpoons 2\,H_2O$	1.23 V
d	$MnO_4^- + 2\,H_2O + 3\,e^- \leftrightharpoons MnO_2 + 4\,OH^-$	0.59 V
e	$H_2O_2 + 2\,H^+ + 2\,e^- \leftrightharpoons 2\,H_2O$	1.78 V
f	$Cr_2O_7{}^{2-} + 14\,H^+ + 6\,e^- \leftrightharpoons 2\,Cr^{3+} + 7\,H_2O$	1.33 V
g	$TEMPO^+ + 2\,H^+ + 2\,e^- \leftrightharpoons TEMPOH_2{}^+$	0.92 V

The catalytic mechanism of TEMPO can be elucidated from a thermodynamic perspective.[6] When using Table 1a as the cathodic half-reaction, the comprehensive electrode potential for the reaction stands at 8.17×10^{-25} V, corresponding to a Gibbs free energy (ΔG) of -1.97 eV. Upon the addition of TEMPO to the solution with reaction Table 1g as the cathodic half-reaction, TEMPO adjusts the electrode potential through its own reduction process, resulting in a decrease in the overall ΔG of the reaction. As a result, this adjustment achieves thermodynamic favorability, reducing the overall ΔG to approximately -2.2×10^{24} eV, which is evident in experimental observations through a lower onset potential in LSV testing. In the realm of traditional oxidation reactions, oxidizing agents like MnO_4^-, H_2O_2, and $Cr_2O_7{}^{2-}$ attain favorable thermodynamics by furnishing rectified redox potentials, as delineated in Table 1d–f. The capacity of TEMPO to facilitate the oxidation of substrates in homogeneous solutions through its own reduction is on par with numerous potent oxidants, albeit without yielding toxic or other adverse stoichiometric byproducts, thereby positioning it as an eco-friendly and efficacious electrocatalytic medium.

Conclusions

The utilization of CuO-NiO as the anode and TEMPO as the electrocatalytic mediator for the synergistic catalysis of LOR achieved high FE of 81.69% in 0.1 M LiOH. This approach avoids the heterogeneous oxidation and the environmental pollution caused by $KMnO_4$. The introduction of a surfactant led to the formation of CuO-NiO nanoparticles with an average diameter of 33.13 nm, exhibiting a spherical nanoscale structure. Additionally, the incorporation of NiO enhanced the

adsorption affinity of substrates and refined the surface charge density, which accelerates the selective oxidation of substrates and enhances reaction kinetics.

TEMPO is initially oxidized by Cu^{2+} and Ni^{3+}, followed by synergistic catalysis of LOR with the CuO-NiO anode. DFT calculations and ATR-FTIR indicate that the active -NH_2 group in LLM-116 couples to form the intermediate -NH-NH- after deprotonation, ultimately dehydrogenating to produce H_2NPA, the crucial step governing substrate oxidation coupling is the formation of compound 2. The essence of TEMPO lowering the reaction potential lies in providing a more favorable reduction potential to decrease the reaction energy, achieving advantageous thermodynamics.

ASSOCIATED CONTENT

Supporting Information

The Supporting Information is available free of charge at https://pubs.acs.org/doi/10.1021/ acssuschemeng.xxxxxxx.

More data on material characterization, electrochemical testing, single crystal structure, DFT calculations, and in-situ infrared testing are attached.

AUTHOR INFORMATION

Corresponding Author

Pengcheng Wang − School of Chemistry and Chemical Engineering, Nanjing University of Science and Technology, Nanjing 210094, China;

https://orcid.org/0000-0002-5282-236X;

Email: alexwpch@njust.edu.cn

Authors

Yuqiu Wang − School of Chemistry and Chemical Engineering, Nanjing University of Science and Technology, Nanjing 210094, China

Guangyuan Zhang − Gansu Yinguang Chemical Industry Group. Co. Ltd, Baiyin 730900. Gansu Province, China

Aijia Tang − School of Chemistry and Chemical Engineering, Nanjing University of Science and Technology, Nanjing 210094, China

Ming Lu − School of Chemistry and Chemical Engineering, Nanjing University of Science and Technology, Nanjing 210094, China

REFERENCES

(1) Yan, M.; Kawamata, Y.; Baran, P. S. Synthetic Organic Electrochemical Methods Since 2000: On the Verge of a Renaissance. *Chem. Rev.* **2017**, 117 (21), 13230–13319. https://doi.org/10.1021/acs.chemrev.7b00397.

(2) Li, L.; Wang, X.; Fu, N. Electrochemical Nickel-Catalyzed Hydrogenation. *Angew. Chemie - Int. Ed.* **2024**, 202403475. https://doi.org/10.1002/ange.202403475.

(3) Barman, K.; Chen, Y.; Wu, S.; Hu, G.; Mirkin, M. V. Voltage-Driven Molecular Catalysis: A Promising Approach to Electrosynthesis. *ACS Catal.* **2023**, 13 (24), 15869–15876. https://doi.org/10.1021/acscatal.3c03644.

(4) Cao, H.; Wang, R.; Zhang, Q.; Lu, C.; Weng, Y.; Gao, M. Electrochemical Oxidative Heterodifunctionalization of Dehydroalanine: Access to Unnatural α,α-Disubstituted Amino Esters. *Org. Chem. Front.* **2024**, 11, 2566–2571. https://doi.org/10.1039/d4qo00193a.

(5) Ucheniya, K.; Jat, P. K.; Chouhan, A.; Yadav, L.; Badsara, S. S. Electrochemical Selective Divergent C-H Chalcogenocyanation of N-Heterocyclic Scaffolds. *Org. Biomol. Chem.* **2024**, 22, 3220–3224. https://doi.org/10.1039/d4ob00448e.

(6) Wang, F.; Stahl, S. S. Electrochemical Oxidation of Organic Molecules at Lower Overpotential: Accessing Broader Functional Group Compatibility with Electron-Proton Transfer Mediators. *Acc. Chem. Res.* **2020**, 53 (3), 561–574. https://doi.org/10.1021/acs.accounts.9b00544.

(7) Sauer, G. S.; Lin, S. An Electrocatalytic Approach to the Radical Difunctionalization of Alkenes. *ACS Catal.* **2018**, 8 (6), 5175–5187. https://doi.org/10.1021/acscatal.8b01069.

(8) Nutting, J. E.; Rafiee, M.; Stahl, S. S. Tetramethylpiperidine N-Oxyl (TEMPO), Phthalimide N-Oxyl (PINO), and Related N-Oxyl Species: Electrochemical Properties and Their Use in Electrocatalytic Reactions. *Chem. Rev.* **2018**, 118 (9), 4834–4885. https://doi.org/10.1021/acs.chemrev.7b00763.

(9) Ma, L.; Gao, X.; Liu, X.; Gu, X.; Li, B.; Mao, B.; Sun, Z.; Gao, W.; Jia, X.; Chen, J. Recent Advances in Organic Electrosynthesis Using Heterogeneous Catalysts Modified Electrodes. *Chinese Chem. Lett.* **2023**, 34 (4), 107735. https://doi.org/10.1016/j.cclet.2022.08.015.

(10) Beejapur, H. A.; Zhang, Q.; Hu, K.; Zhu, L.; Wang, J.; Ye, Z. TEMPO in Chemical Transformations: From Homogeneous to Heterogeneous. *ACS Catal.* **2019**, 9 (4), 2777–2830. https://doi.org/10.1021/acscatal.8b05001.

(11) Lennox, A. J. J.; Nutting, J. E.; Stahl, S. S. Selective Electrochemical Generation of Benzylic Radicals Enabled by Ferrocene-Based Electron-Transfer Mediators. *Chem. Sci.* **2018**, 9 (2), 356–361. https://doi.org/10.1039/c7sc04032f.

(12) Wang, F.; Rafiee, M.; Stahl, S. S. Electrochemical Functional-Group-Tolerant Shono-Type

Oxidation of Cyclic Carbamates Enabled by Aminoxyl Mediators. *Angew. Chemie - Int. Ed.* **2018**, 57 (22), 6686–6690. https://doi.org/10.1002/anie.201803539.

(13) Rafiee, M.; Miles, K. C.; Stahl, S. S. Electrocatalytic Alcohol Oxidation with TEMPO and Bicyclic Nitroxyl Derivatives: Driving Force Trumps Steric Effects. *J. Am. Chem. Soc.* **2015**, 137 (46), 14751–14757. https://doi.org/10.1021/jacs.5b09672.

(14) Zhou, J.; Ma, Z. Y.; Shonhe, C.; Ji, S. H.; Cai, Y. R. TEMPO-Catalyzed Electrochemical Dehydrogenative Cyclocondensation of: O -Aminophenols: Synthesis of Aminophenoxazinones as Antiproliferative Agents. *Green Chem.* **2021**, 23 (21), 8566–8570. https://doi.org/10.1039/d1gc02908h.

(15) Lv, H.; Laishram, R. D.; Yang, Y.; Li, J.; Xu, D.; Zhan, Y.; Luo, Y.; Su, Z.; More, S.; Fan, B. TEMPO Catalyzed Oxidative Dehydrogenation of Hydrazobenzenes to Azobenzenes. *Org. Biomol. Chem.* **2020**, 18 (18), 3471–3474. https://doi.org/10.1039/d0ob00103a.

(16) Fang, C.; Li, M.; Hu, X.; Mo, W.; Hu, B.; Sun, N.; Jin, L.; Shen, Z. A Mild TEMPO-Catalyzed Aerobic Oxidative Conversion of Aldehydes into Nitriles. *Adv. Synth. Catal.* **2016**, 358 (7), 1157–1163. https://doi.org/https://doi.org/10.1002/adsc.201501130.

(17) Fukuda, N.; Izumi, M.; Ikemoto, T. Safe and Convenient Nitroxyl Radical and Imide Dual Catalyzed NaOCl Oxidation of Alcohols to Aldehydes/Ketones. *Tetrahedron Lett.* **2015**, 56 (25), 3905–3908. https://doi.org/10.1016/j.tetlet.2015.04.115.

(18) Könning, D.; Olbrisch, T.; Sypaseuth, F. D.; Tzschucke, C. C.; Christmann, M. Oxidation of Allylic and Benzylic Alcohols to Aldehydes and Carboxylic Acids. *Chem. Commun.* **2014**, 50 (39), 5014–5016. https://doi.org/10.1039/c4cc01305k.

(19) Ryan, M. C.; Whitmire, L. D.; McCann, S. D.; Stahl, S. S. Copper/TEMPO Redox Redux: Analysis of PCET Oxidation of TEMPOH by Copper(II) and the Reaction of TEMPO with Copper(I). *Inorg. Chem.* **2019**, 58 (15), 10194–10200. https://doi.org/10.1021/acs.inorgchem.9b01326.

(20) Heard, D. M.; Lennox, A. J. J. Electrode Materials in Modern Organic Electrochemistry. *Angew. Chemie - Int. Ed.* **2020**, 59 (43), 18866–18884. https://doi.org/10.1002/anie.202005745.

(21) Nam, D. H.; Taitt, B. J.; Choi, K. S. Copper-Based Catalytic Anodes to Produce 2,5-Furandicarboxylic Acid, a Biomass-Derived Alternative to Terephthalic Acid. *ACS Catal.* **2018**, 8 (2), 1197–1206. https://doi.org/10.1021/acscatal.7b03152.

(22) Vu, H. K.; Mahvelati-Shamsabadi, T.; Dang, T. T.; Hur, S. H.; Kang, S. G.; Chung, J. S. Synergistic Effects of Ni and Cu in Morphology-Controlled NiCu Electrocatalysts for Ammonia Electro-Oxidation. *ACS Appl. Nano Mater.* **2023**, 6 (22), 20688–20699. https://doi.org/10.1021/acsanm.3c03422.

(23) Ma, Y.; Zhao, Z.; Zhang, C.; Zhang, Y.; Zhang, C.; Li, J.; Xu, M.; Ma, H. Synergistic Reaction Kinetics of Pt Single Atoms/MoS2 and Nanoparticles for Energy-Saving Hydrogen Production Assisted by Green Electrosynthesis of Azotetrazolate Compound. *Chem. Eng. J.* **2023**, 475, 146303. https://doi.org/10.1016/j.cej.2023.146303.

(24) Li, J.; Ma, Y.; Zhang, C.; Zhang, C.; Ma, H.; Guo, Z.; Liu, N.; Xu, M.; Ma, H.; Qiu, J. Green Electrosynthesis of 3,3'-Diamino-4,4'-Azofurazan Energetic Materials Coupled with Energy-Efficient Hydrogen Production over Pt-Based Catalysts. *Nat. Commun.* **2023**, 14 (1), 1–15. https://doi.org/10.1038/s41467-023-43698-x.

(25) Wu, J.; Zhai, Z.; Yin, S.; Wang, S. General Formation of Interfacial Assembled Hierarchical Micro-Nano Arrays for Biomass Upgrading-Coupled Hydrogen Production. *Adv. Funct. Mater.*

2024, 34 (6), 1–10. https://doi.org/10.1002/adfm.202308198.

(26) Li, Q.; Guo, X.; Wang, J.; Pang, H. Construction of Hierarchical Nanostructures and NiO Nanosheets@nanorods for Efficient Urea Electrooxidation. *Chinese Chem. Lett.* **2023**, 34 (7), 107831. https://doi.org/10.1016/j.cclet.2022.107831.

(27) Tang, Y.; Gao, H.; Yang, M.; Wang, G.; Li, J.; Zhang, H.; Tao, Z. NiO Promoted CuO-NiO/SBA-15 Composites as Highly Active Catalysts for Epoxidation of Olefins. *New J. Chem.* **2016**, 40 (10), 8543–8548. https://doi.org/10.1039/c6nj01654e.

(28) Zhang, M.; Fu, W.; Li, C.; Gao, H.; Tang, L.; Zhou, Z. (E)-1,2-Bis(3,5-Dinitro-1H-Pyrazol-4-yl) diazene – Its 3D Potassium Metal–Organic Framework and Organic Salts with Super-Heat-Resistant Properties. *Eur. J. Inorg. Chem.* **2017**, 2017 (22), 2883–2891. https://doi.org/10.1002/ejic.201700001.

(29) Schmidt, R. D.; Lee, G. S.; Pagoria, P. F.; Mitchell, A. R. Synthesis and Properties of a New Explosive, 4-Amino-3,5-Dinitro-1H-Pyrazole (LLM-116). *J. Heterocycl. Chem.* **2001**, 38, 1227–1230.

(30) Ko, Y. J.; Han, M. H.; Kim, H.; Kim, J. Y.; Lee, W. H.; Kim, J.; Kwak, J. Y.; Kim, C. H.; Park, T. E.; Yu, S. H.; Lee, W. S.; Choi, C. H.; Strasser, P.; Oh, H. S. Unraveling Ni-Fe 2D Nanostructure with Enhanced Oxygen Evolution via in Situ and Operando Spectroscopies. *Chem Catal.* **2022**, 2 (9), 2312–2327. https://doi.org/10.1016/j.checat.2022.07.016.

(31) Li, F.; Chang, X.; Wang, S.; Guo, Y.; Li, H. Y.; Wu, K. Excellent Electrocatalytic Performance toward Methanol Oxidation of Hierarchical Porous NiCu Obtained by Electrochemical Dealloying. *J. Alloys Compd.* **2023**, 934, 167811. https://doi.org/10.1016/j.jallcom.2022.167811.

(32) Khan, S. B.; Asiri, A. M. Copper Oxide Doped Composite Nanospheres Decorated Graphite Pencil toward Efficient Hydrogen Evolution Electrocatalysis. *J. Mol. Liq.* **2021**, 335, 116084. https://doi.org/10.1016/j.molliq.2021.116084.

(33) Ahsan, M. A.; Puente Santiago, A. R.; Hong, Y.; Zhang, N.; Cano, M.; Rodriguez-Castellon, E.; Echegoyen, L.; Sreenivasan, S. T.; Noveron, J. C. Tuning of Trifunctional NiCu Bimetallic Nanoparticles Confined in a Porous Carbon Network with Surface Composition and Local Structural Distortions for the Electrocatalytic Oxygen Reduction, Oxygen and Hydrogen Evolution Reactions. *J. Am. Chem. Soc.* **2020**, 142 (34), 14688–14701. https://doi.org/10.1021/jacs.0c06960.

(34) Zhou, P.; Lv, X.; Tao, S.; Wu, J.; Wang, H.; Wei, X.; Wang, T.; Zhou, B.; Lu, Y.; Frauenheim, T.; Fu, X.; Wang, S.; Zou, Y. Heterogeneous-Interface-Enhanced Adsorption of Organic and Hydroxyl for Biomass Electrooxidation. *Adv. Mater.* **2022**, 34 (42), 1–9. https://doi.org/10.1002/adma.202204089.

(35) Yan, Y.; Wang, R.; Zheng, Q.; Zhong, J.; Hao, W.; Yan, S.; Zou, Z. Nonredox Trivalent Nickel Catalyzing Nucleophilic Electrooxidation of Organics. *Nat. Commun.* **2023**, 14 (1), 1–11. https://doi.org/10.1038/s41467-023-43649-6.

(36) Roy, A.; Ray, A.; Saha, S.; Ghosh, M.; Das, T.; Nandi, M.; Lal, G.; Das, S. Influence of Electrochemical Active Surface Area on the Oxygen Evolution Reaction and Energy Storage Performance of MnO2-Multiwalled Carbon Nanotube Composite. *Int. J. Energy Res.* **2021**, 45 (11), 16908–16921. https://doi.org/10.1002/er.6885.

(37) Nishijima, M.; Sasano, Y.; Iwabuchi, Y.; Araki, Y. Comprehensive Structural and Electronic Properties of 2-Azaadamantane N-Oxyl Derivatives Correlated with Their Catalytic Ability. *ACS Omega* **2023**, 8 (51), 49067–49072. https://doi.org/10.1021/acsomega.3c06902.

(38) Shibuya, M.; Tomizawa, M.; Suzuki, I.; Iwabuchi, Y. 2-Azaadamantane N-Oxyl (AZADO)

and 1-Me-AZADO: Highly Efficient Organocatalysts for Oxidation of Alcohols. *J. Am. Chem. Soc.* **2006**, 128 (26), 8412–8413. https://doi.org/10.1021/ja0620336.

(39) Bobbitt, J. M.; BrüCkner, C.; Merbouh, N. Oxoammonium- and Nitroxide-Catalyzed Oxidations of Alcohols. *Org. React.* **2009**, 103–424. https://doi.org/10.1002/0471264180.or074.02.

(40) Lemaitre, S.; Romain, A. L.; Bariere, F.; Craquelin, A.; Copin, C.; Jean, A. Development and Pilot Scale Implementation of Safe Aerobic Cu/TEMPO Oxidation in a Batch Reactor. *Green Chem.* **2023**, 25 (14), 5698–5711. https://doi.org/10.1039/d3gc00579h.

(41) Lima, M. A. S.; Raimundo, R. A.; Araújo, A. J. M.; Oliveira, J. F. G. d. A.; Loureiro, F. J. A.; Macedo, D. A.; Morales, M. A. Nickel-Copper-Carbon Based Electrocatalysts for Oxygen Evolution Reaction: Sol-Gel Synthesis Using Chitosan. *Int. J. Hydrogen Energy* **2024**, 51, 663–675. https://doi.org/10.1016/j.ijhydene.2023.08.287.

(42) Zhang, Y.; Ma, D.; Lei, Y.; Zhu, T.; Hu, J.; Tang, Y.; Chen, Z.; Huang, J.; Lai, Y.; Lin, Z. Markedly Enhanced Hydrogen Production in Wastewater via Ammonia-Mediated Metal Oxyhydroxides Active Sites on Bifunctional Electrocatalysts. *Nano Energy* **2023**, 117, 108896. https://doi.org/10.1016/j.nanoen.2023.108896.

(43) Zhao, C.-X.; Liu, J.-N.; Li, B.-Q.; Ren, D.; Chen, X.; Yu, J.; Zhang, Q. Multiscale Construction of Bifunctional Electrocatalysts for Long-Lifespan Rechargeable Zinc–Air Batteries. *Adv. Funct. Mater.* **2020**, 30 (36), 2003619. https://doi.org/https://doi.org/10.1002/adfm.202003619.

(44) Ma, W.; Xie, S.; Liu, T.; Fan, Q.; Ye, J.; Sun, F.; Jiang, Z.; Zhang, Q.; Cheng, J.; Wang, Y. Electrocatalytic Reduction of CO2 to Ethylene and Ethanol through Hydrogen-Assisted C–C Coupling over Fluorine-Modified Copper. *Nat. Catal.* **2020**, 3 (6), 478–487. https://doi.org/10.1038/s41929-020-0450-0.

(45) Chen, D.; Ding, Y.; Cao, X.; Wang, L.; Lee, H.; Lin, G.; Li, W.; Ding, G.; Sun, L. Highly Efficient Biomass Upgrading by a Ni−Cu Electrocatalyst Featuring Passivation of Water Oxidation Activity. *Angew. Chemie - Int. Ed.* **2023**, 62 (37), e202309478. https://doi.org/10.1002/anie.202309478.

(46) Lin, R.; Ke, C.; Chen, J.; Liu, S.; Wang, J. Asymmetric Donor-Acceptor Molecule-Regulated Core-Shell-Solvation Electrolyte for High-Voltage Aqueous Batteries. *Joule* **2022**, 6 (2), 399–417. https://doi.org/10.1016/j.joule.2022.01.002.

(47) Zhou, P.; Lv, X.; Huang, H.; Cheng, B.; Zhan, H.; Lu, Y.; Frauenheim, T.; Wang, S.; Zou, Y. Construction of Ag─Co(OH)$_2$ Tandem Heterogeneous Electrocatalyst Induced Aldehyde Oxidation and the Co-Activation of Reactants for Biomass Effective and Multi-Selective Upgrading. *Adv. Mater.* **2024**, 2312402, 1–11. https://doi.org/10.1002/adma.202312402.